Local complex reflectivity in optical waveguides

A. Bruyant,[*] G. Lerondel,[†] S. Blaize, I. Stefanon, S. Aubert, R. Bachelot, and P. Royer

Laboratoire de Nanotechnologie et Instrumentation Optique, CNRS (FRE 2671), Universite de Technologie de Troyes, 10010 TROYES cedex, France[‡]

With the aim of probing the photonic band structure of waveguiding micro- and nanooptical devices, we re-introduce the modal local complex reflectivity (LCR) and review the impact of scanning near-field optical microscopy (SNOM) methods on the determination of LCR in such devices. These methods include intensity and complex field mapping of standing waves, as a function of the wavelength. A unified treatment of the LCR probing is given for both standard SNOM and phase sensitive SNOM. Experimental demonstration of these two methods on several microstructured devices (Bragg grating structures) is done using a scattering-type SNOM whose specific advantages in terms of resolution and accuracy are addressed. The phase sensitive version of the scattering-type SNOM is shown to be very well suited for LCR measurement as well as general modal and dispersion analysis. The possibility to obtain the scattering matrix of micro- and nanodevices as a function of the wavelength is foreseen by using the described microscope.

I. INTRODUCTION

The usual reflectivity spectra $R(\lambda) = |r(\lambda)|^2$ of photonic structures such as photonic crystals or optical integrated devices are only imperfect signatures of their optical band structures. Mainly, the phase related to the complex coefficient $r(\lambda)$ cannot generally be retrieved from the only amplitude response.[1] However, the phase information is very important since it directly gives the group delay $\tau(\lambda)$, which quantifies the dispersion of the optical component. Knowledge of the complex response in reflection or transmission is hence of crucial importance for the design and the optimization of dispersive optical devices including fiber Bragg grating dispersion compensators and filters,[2–4] absorbing reflector,[5] microcavity and other slow wave structures,[6,7] delay line, etc. Even for nonresonant structures, such as splitter waveguides or multimode interferometer (MMI),[8] the phase information naturally allows for a more detailed analysis of the given structure.

During the last decades many different "black-box-type" methods have been proposed to experimentally obtain the complex reflectivity or transmissivity. These methods include phase-shift methods,[9,10] pulse delay methods,[11] and cw-interferometric methods using low[12–15] or high coherence sources.[16]

All these experimental methods allow one to retrieve the complex response of an optical component located far from the detection system. The measured group delays or phases correspond solely to the delay associated with a localized and distant feature, for example a small isolated corrugation on an optical chip. However, one important problem is that the complex optical response of numerous components may be involved in an optical chip. Although it is possible to retrieve the whole complex response of the system, it may be difficult to nondestructively discriminate the complex spectral signature of each element if the components are closed to each other. This limitation is due to the finite spatial resolution of the techniques and the multiple path problems. Even if experiments such as low coherence reflectometry may en-

able to probe overlapping complex spectral responses of cascaded components, this task is only possible if one knows that the effective spatial separation exceeds the width of the individual interferometric signatures.[17] In addition, every element induces small or important optical losses that irremediably affect the amplitude signal. This last point is a general limitation of all the above-mentioned methods. To avoid the intrinsic averaging of these black-box-type techniques, new local techniques are being developed for the characterization of photonic chips. As a beautiful example, the pulse delay method has recently been combined with phase sensitive scanning-near-field optical microscopy (SNOM),[18] in order to locally study the dispersion properties of photonic crystal waveguides.[19] Several others techniques based on tunable coherent sources[20–22] or low coherence sources can also be investigated for local dispersion measurements.

We have recently introduced a method to retrieve the complex response of Bragg grating devices, which utilizes a SNOM in combination with a highly coherent tunable source.[20,21] The basic idea of the method is to map the field intensity prior to the reflection zone under study. The analysis of the standing waves as a function of the wavelength enables one to determine the local complex reflection coefficient of the whole structure located after the scanning area. Experimentally, intensity mapping was performed with a specific scanning near-field optical microscope: a scattering-type SNOM (s-SNOM). Local complex reflectivity (LCR) probing using standing-wave imaging is actually a general approach that could be applied to many kinds of photonic structures. The current paper intends to describe further and generalize this approach.

After introducing the concept of LCR and LCR retrieval by SNOM (Sec. II) as well as the experimental approach used to retrieve the LCR (Sec. III), complex reflectivity spectra obtained on different kinds of gratings structures are presented and discussed (Sec. IV). In particular, we show how by combining s-SNOM with a heterodyne interferometric detection the LCR can be determined through complex field mapping (amplitude and phase) of the standing waves. In Secs. II and III, the effect of the optical resolution on the

LCR normalization and the motivations for using scattering-type near-field optical microscope are, respectively, addressed and presented. More details about the signal detected by an s-SNOM are given in the Appendix.

II. THEORETICAL ASPECTS

A. Local complex reflection coefficient definition

In order to define the local complex reflectivity retrieved by our SNOM experiment, we consider a single-mode optical waveguide located in an optical chip. In the simplest case, this section may be located just prior to a single functional device but more generally, it may be located between two devices, where multiple reflection may occur. We further assume that the scalar theory is applicable, by considering that the forward and backward mode is mainly linearly polarized in the transverse plane (y,z).[50] The total field $E=E_y$ or $E=E_z$ can then be expressed as

$$E(x,y,z) = E^+(x,y,z) + E^-(x,y,z), \quad (1)$$

with

$$E^{\pm}(x,y,z) = A^{\pm}\psi(y,z)e^{\mp i\beta x}, \quad (2)$$

where $\psi(y,z)$ is the normalized field distribution having a real propagation constant β. The complex field amplitudes $A^{\pm}$ define the amplitude ratio between the two guided modes in x, as well as an eventual phase shift additional to the propagation phase term $\mp i\beta x$. A local complex reflection coefficient at an x position prior to the functional device of interest can then be defined as

$$r(x,\beta) = \frac{E^-(x,y,z)}{E^+(x,y,z)} = \frac{A^-}{A^+}e^{i2\beta x}. \quad (3)$$

This coefficient describes the equivalent reflector by which the whole structure after x could be replaced and corresponds to the local complex reflectivity when the wavelength is varied. More generally, we could put $r(x,\beta)$ in a matrix form in order to distinguish between all the field components. With our scalar hypothesis, this ratio is a complex number with the phase term accounting for the relative phase delay between $E^-(x,y,z)$ and $E^+(x,y,z)$ in x. At least, we should note that the local reflectivity we have defined is essentially a valid concept for modal reflectivity under the condition that there is no ambiguity in the optical path. Hence for an unbounded waveguide where the light has a non-negligible angular distribution, the concept of local reflectivity would be more difficult to handle since the light is distributed on a wide surface. Nevertheless, the concept of LCR can still be handled for a continuum of modes as far as the impinging and reflected light have a negligible angular distribution (such as leaky modes, cf. Sec. IV B 4). This is *a fortiori* the case for multimode bounded structures.

Several general and simple remarks can be made in order to get a physical understanding of the method that we propose for the LCR retrieval. In the following, we will investigate sufficiently small zones, so that the amplitude of $r(x,\beta)$ at a given wavelength can be considered as quasiconstant (lossless waveguide). This approximation is important because practically, we will retrieve the LCR value by a spatial Fourier analysis of the signal. If the LCR varies notably in this zone, the procedure will average its value. On the other hand, the phase value depends on the phase shift induced by the reflection(s) but also on the x position inside this zone. From Eq. (3), the propagation equations of $r(x,\beta)$ and its phase $\Delta\phi(x,\beta)$ can then be explicitly written as

$$r(x,\beta) = r(0,\beta)e^{2i\beta x}, \quad (4)$$

$$\Delta\phi(x,\beta) = \Delta\phi(0,\beta) + 2\beta x, \quad (5)$$

where $x=0$ is an arbitrary origin inside the investigated zone. For a real-space investigation, it is also useful to express the phase of $r(x,\beta)$ as a distance between the considered position x and an effective reflection point x_{eff}:

$$\Delta\phi(x,\beta) = 2\beta(x_{eff} - x). \quad (6)$$

In the case of a single interface, the effective or phase length $l_{eff}=x_{eff}-x$ is constant. This length corresponds to the physical distance between this interface and the measurement point, if the Fresnel reflection induces a zero phase shift. More generally, l_{eff} depends on the wavelength. For a multilayer structure, the effective length strongly varies if the wavelength is detuned from the Bragg resonance. To emphasize this point, Fig. 1 shows the complex reflectivity spectrum $r(0,\beta)$ of a multilayered structure, calculated by Rouard's method.[23–25] Figure 1(b) presents the LCR amplitude before the reflector, and Fig. 1(c) presents its phase at the grating front, as a function of the wavelength λ_0. The corresponding *ad hoc* structure used for this simple simulation is shown in Fig. 1(d). The standing waves appearing just prior to the Bragg mirror are also given as a function of the wavelength in the same figure [Fig. 1(a)].

We can note from the phase variations [Fig. 1(c)] that the effective distance $l_{eff}=x_{eff}-x$ is nearly constant and minimal inside the stop band, where the light less penetrates the structure. For these particular cases where the effective length is slowly varying with β and in the absence of additional dispersion of the effective index, the effective length corresponds to the group length $l_g=\tau(\lambda)c$, where the local group delay in reflection, $\tau(\lambda)$ is given by

$$\tau(\lambda) = \frac{1}{(2\pi c)}\frac{d\Delta\phi}{d\sigma}, \quad (7)$$

with c, the speed of light in vacuum and σ the wave number. In other words, a constant effective length simply means that the phase velocity of the reflected guided mode is equal to its group velocity and that no dispersion occurs from the grating. On the other hand, close to the band edges and close to the other reflection minima, the phase length in reflection l_{eff} and the group delay increases dramatically and are no more defined on the zero of the LCR. In the experimental part of this paper, we will consider the particular case of a constant effective length as well as the more general case of a variable effective length.
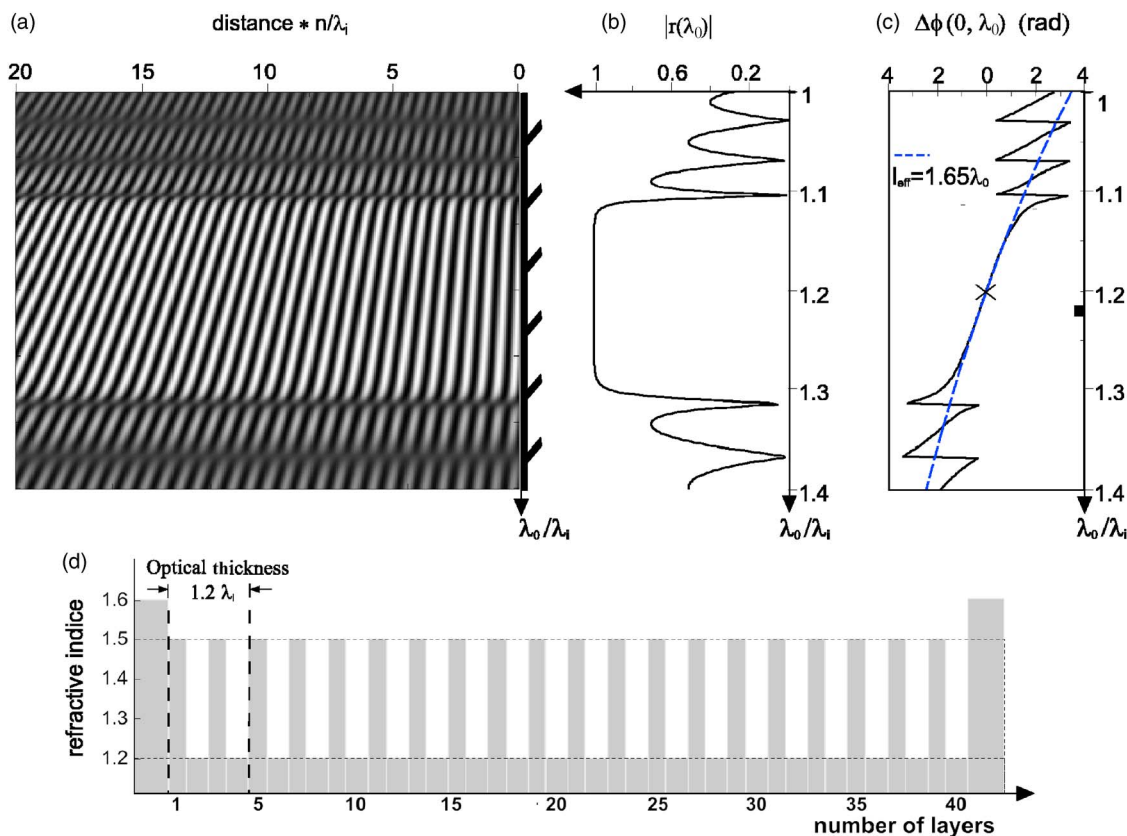
FIG. 1. (Color online) (a) Simulation of a standing-wave pattern formed along the x direction as a function of λ_0, in front of a given multilayer structure. A single incident mode with an optical constant $\beta = n2\pi/\lambda_0$ is considered here. (b) Amplitude of the complex reflection coefficient of the multilayer structure. (c) Phase $\Delta\phi(0,\lambda_0)$ of the complex reflection coefficient at the multilayer front interface. The point matching exactly the Bragg condition is marked with a cross. Inside the plateau, the phase exhibits a typical variation (proportional to β) corresponding to a unique interface positioned at $1.65\lambda_i$ after the front interface (dashed line). (d) Index profile of the given multilayer made of 40 quarter wavelength stacks.

B. Intensity analysis of the standing waves

Let us consider the local intensity profiles $I(x,\beta)$ of the standing waves, in a given position (y_o, z_o) above the wave-guide top surface. This intensity can be explicitly expressed as a function of the LCR amplitude $|r(x,\beta)|$ and phase $\Delta\phi(x,\beta)$ as

$$I(x,\beta) = |A^+|^2 |\psi(y_o,z_o)|^2 * [1 + |r(x,\beta)|^2$$
$$+ 2|r(x,\beta)|\cos(\Delta\phi(x,\beta))]. \quad (8)$$

A simple way to estimate the LCR amplitude consists then in reading the contrast of the measured standing waves as performed by Flück *et al.*[26] The contrast defined by

$$C = \frac{I_{max}(x) - I_{min}(x)}{I_{max}(x) + I_{min}(x)} = \frac{2|r(x)|}{|r(x)|^2 + 1} \quad (9)$$

leads to the amplitude value of the LCR:

$$|r(x)| = (1 - \sqrt{1 - C^2})/C. \quad (10)$$

Figure 1(a) is an example of a standing-wave pattern formed in front of the mirror shown in Fig. 1(d) as a function of x and λ_0. From such a standing-wave spectrum (SWS), the contrast values determined for each wavelength theoretically

enable us to retrieve the LCR amplitude spectrum with an error depending on the optical resolution. Moreover, the evolution of the phase $\Delta\phi$ can also be directly read on the SWS at a given x position. From an experimental point of view, one drawback of this purely real-space method to determine the local LCR spectrum is its sensitivity to the possible experimental noise.

To overcome this specific difficulty, the spatial Fourier transform (FT) of the standing-wave spectrum can be used. For a given λ_0, the Fourier transform of Eq. (8) is given by

$$F_I(f_x) = |A^+|^2 |\psi(y_o,z_o)|^2 * \{[1 + |r(x)|^2]\delta(f_x) + |r(x)|$$
$$* [e^{-i2\beta x_{eff}}\delta(f_x - 2\beta_x) + e^{i2\beta x_{eff}}\delta(f_x + 2\beta_x)]\}. \quad (11)$$

From the peak amplitude $|F_I(2\beta)|$, the reflection coefficient amplitude $|r(x)|$ can be retrieved, whereas the phase $\arg[F_I(2\beta)]$ will give the phase value $\Delta\phi(x)$ measured at the center of the standing-wave profile. Now, repeating this procedure for each wavelength, the LCR spectrum of the whole structure located after the measurement point (e.g., the system formed by the grating and the exit facet) is obtained.

Figure 2(a) shows the original LCR of the simulated structure and the LCR retrieved from a spatial fast Fourier
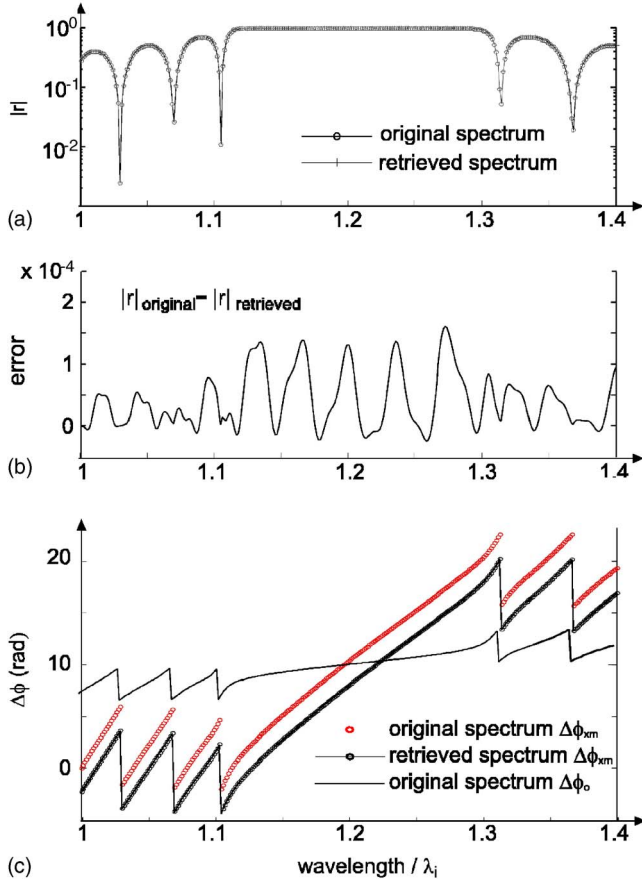
FIG. 2. (Color online) Comparison between the theoretical LCR (Rouard's method) and the LCR numerically retrieved from the associated standing-wave spectrum (see Fig. 1). (a) Amplitudes of both LCR in logarithmic scale and related error (b). (c) Phases of the LCR at the front interface ($\Delta\phi_o$) and at the measurement point ($\Delta\phi_{xm}$), i.e., at the center of the standing-wave profile. Measured and retrieved spectra of $\Delta\phi_{xm}$ have been separated for a better comparison. They present a greater angular extension due to the additional propagation between the measurement point and the grating.

transform of the simulated standing-waves spectrum. The retrieved amplitude spectrum is very similar to the initial one as shown by the error spectrum in Fig. 2. Note that to avoid a spectral dispersion of the standing-wave peaks on the Fourier transform amplitude, it is useful to apply a Hamming window on the SWS. By taking into account the propagation between the grating and the center of the standing-wave profile, a very good agreement can also be found on the phase spectra [Fig. 2(c)]. A greater extension of the LCR phase at the standing-wave center ($\Delta\phi_{xm}$) can be seen, compared to the LCR phase at the grating front ($\Delta\phi_0$). The additional propagation from the measurement point to the grating ($10\lambda_i/n$) entails this additional variation which corresponds to a linear slope in the frequency domain.

Beside the necessity for high optical resolution, the complex response retrieval by intensity mapping presents several limitations. First, the analysis becomes difficult when dealing with multimode structures. Second, the complex transmissivity cannot be investigated in this way. These two problems can be solved by analyzing the complex field with a phase

sensitive setup. This second method is presented below and the experimental setup is described in the next section.

C. Complex field analysis of the standing waves

Using a phase sensitive SNOM, it is possible to retrieve both the amplitude and the phase of the local field. Such experiments have already been carried out on standing waves, for example, on a prism[27] or in a guided configuration.[28] Let us remind of the complex field expression in the case of a single guided mode propagating and being reflected along the X direction. Omitting the field distribution in the (y,z) plane, the field before the reflection zone can be expressed as

$$E(x,\beta) = A^+ e^{-i\beta x}[1 + r(x,\beta)], \quad (12)$$

where, as defined previously, A^+ is the complex amplitude of the impinging guided mode at a given position. The amplitude and the phase of the total field for a given optical constant β can be expressed as

$$\begin{cases} |E(x)| = |A^+|[1 + |r(x)|^2 + 2|r(x)|\cos(\Delta\phi_x)]^{1/2} \\ \Phi(x) = \phi^+ - \beta x + a\tan\left(\dfrac{|r(x)|\sin(\Delta\phi_x)}{1 + |r(x)|\cos(\Delta\phi_x)}\right), \end{cases} \quad (13)$$

where ϕ^+ is the phase term of the complex amplitude of the guided mode A^+ and where the last term corresponds to $\arg(1+r)$. Figure 3 shows the amplitude and the phase profiles for different values of $|r(x)|$. When the reflection is equal to zero, $\Phi(x)$ has a linear variation, $\Phi(x) = \phi^+ - \beta x$. For $|r(x)| \neq 0$, $\Phi(x)$ has an additional periodic variation and for $|r(x)| = 1$, the maximum amplitude of this periodic term is π. In this case, $\Phi(x)$ exhibits a characteristic step profile.

The complex values of $r(x,\beta)$ can then be estimated from the standing-wave profiles in amplitude $|E(x)|$ and in phase $\Phi(x)$, obtained at different wavelengths. But the complex coefficient $|r(x,\beta)|$ can also be estimated for each β with the Fourier transform of the total complex field $E(x)$:

$$F_E(f_x) = A^+\delta(f_x - \beta) + |r(x)|A^+ e^{i\beta x_{eff}}\delta(f_x + \beta). \quad (14)$$

This method offers a simple way to separately estimate from $F_E(\beta)$ and $F_E(-\beta)$ the phases and the amplitudes of the forward and backward guided modes, respectively. The same method could be applied not only before a device but also after a device in order to obtain the complex transmissivity or the scattering matrix of the structure.

D. Optical resolution and normalization

Due to the finite size of the tip, the absolute value $|r(x)|$ is generally difficult to retrieve. Experimentally, a decrease of the standing-wave contrast is often observed by using even slightly coated fiber probes (for example, this can be seen by comparing the PSTM measurements in Ref. 29 on Bragg grating structures with observations in back reflection[30]). Such a behavior was also reported in early experiments (see, for example, the description in Ref. 31 and references therein). A simple way to account for these decreases is to integrate the field intensity over the probe area. The
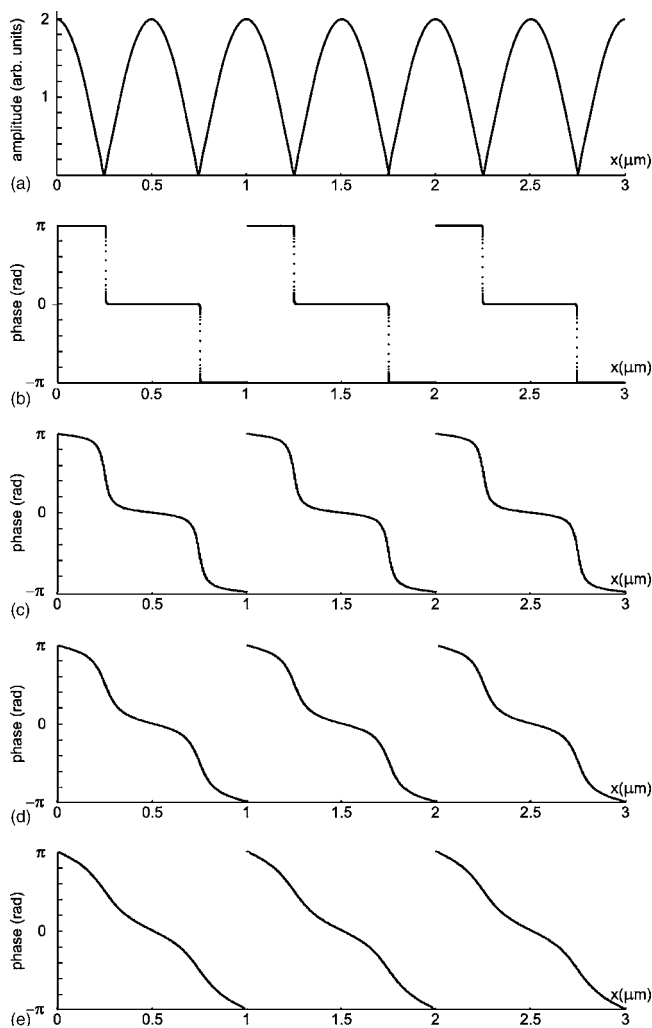
FIG. 3. Simulated amplitude $|E(x)|$ and phase $\Phi(x)$ profiles. (a) Amplitude and phase for a reflection coefficient close to 1 [$|r(x)|$ =0.999] and phase profiles for (b) $|r(x)|$=0.75, (c) $|r(x)|$=0.50, and (d) $|r(x)|$=0.25.
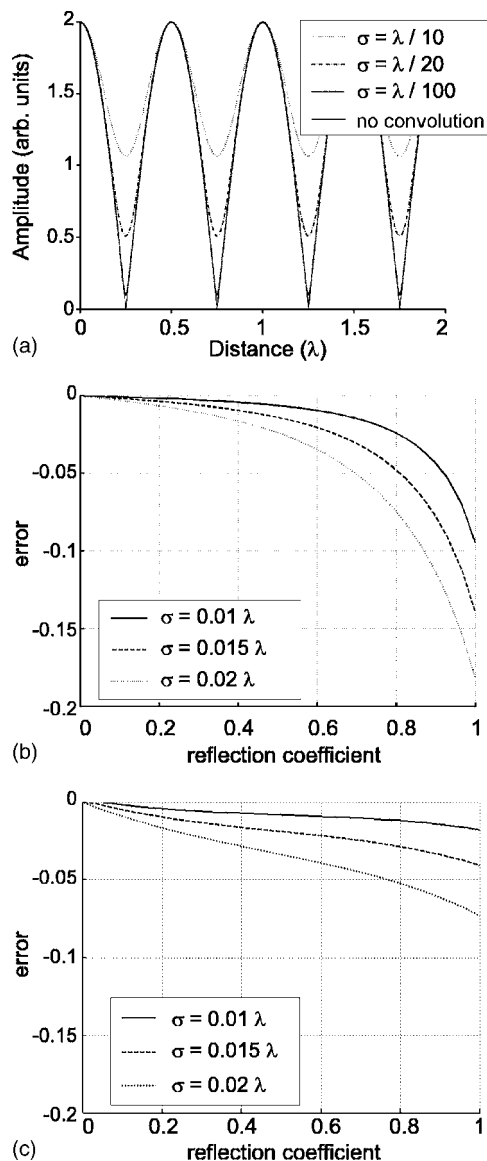

FIG. 4. Effect of a Gaussian convolution on the standing-wave profile and related error. (a) Standing wave obtained for $|r(x)|$=1 without convolution and convolved with a Gaussian function for different standard deviations σ (in unit of $\lambda=2\pi/\beta$). (b) Error obtained on $|r(x)|$ from the contrast measurement as a function of $|r(x)|$ and for different standard deviations. (c) Error on $|r(x)|$ by Fourier analysis of the complex field, both phase and amplitude being convolved (not the complex field).

standing-wave contrast or the peak amplitude $|F_I(2\beta_x)|$ is then substantially underestimated especially in the case of a strong reflection.

It has to be noted, however, that from a theoretical point of view, a decrease in the standing-wave contrast is not necessarily expected as explained and discussed in Refs. 31 and 32. Another fast demonstration of this statement can be done by convolving the *complex* field profile of the standing wave with any symmetric complex function. The result is that the contrast remains unchanged. Hence a good evaluation of the contrast could always be obtained as far as the detection is kept perfectly symmetric and based on the assumption of a passive probe. However, practically, it is likely that for a reasonably symmetric and wide probe, the signal is finally averaged because the scattering process becomes more complex when the size of the the probe is no longer small compared to the wavelength.

As an illustration, Fig. 4(a) shows the amplitude field profile for $|r(x)|$=1 and the effect of a Gaussian convolution on the profiles. The real field amplitude exhibits a sharp profile

close to the nodes. When the signal is slightly averaged the resulting SW profile leads to an underestimated value of $|r(x)|$. The error made on $|r(x)|$ using the contrast of the amplitude profiles is plotted in Fig. 4(b) as a function of $|r(x)|$ and for different "tip radius." (Typical aperture radius is in the order of $\lambda/20$ in the visible or NIR range.)

The error obtained using a Fourier analysis of the complex field profiles when amplitude and phase are convolved is shown in Fig. 4(c). We can note that for a strong reflection the determination of $|r(x)|$ with the complex fields profile is more precise [see Fig. 4(c)]. However, in both cases a resolution close to $\lambda/100$ seems necessary to reach high reflec-
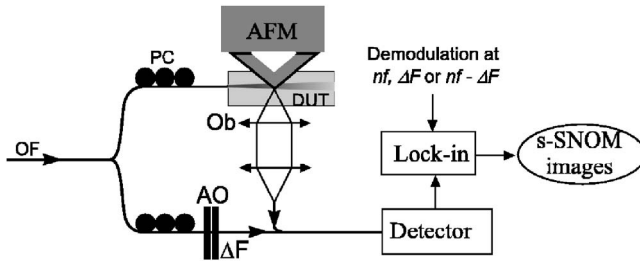
FIG. 5. s-SNOM experimental setup scheme based on a Mach-Zehnder configuration (top view). OF: single-mode optical fiber; PC: polarization controller; DUT: device under test; AFM: atomic force microscope; AO: acousto-optic modulators; Ob: objective of the confocal microscope; f: vibration frequency of the probe; ΔF: optical frequency shift induced by the AO.

tion values. Note now that if the complex field is directly convolved with a symmetric complex function, no discrepancy in the contrast is observed (not shown in the figure), which is no more true if the complex function is asymmetric.

From these simple considerations, the best configuration to reach a correct value of the reflection coefficient from a measured SW contrast is to have the smallest possible optical probe (pointlike) together with a symmetric detection of the field scattered by such a probe. This point is actually a strong motivation for the scattering-type SNOM experimental approach described hereafter.

III. EXPERIMENTAL APPROACH

A. Motivations for the s-SNOM approach

The SNOM is now a widely known tool for the characterization of optical integrated devices. In this technique, a coated or uncoated tapered optical fiber is usually used to collect locally both the evanescent light of the confined modes and the radiation modes.[33] When the SNOM is combined with an interferometric heterodyne detection, it can provide precise information about the local complex field, allowing a direct analysis of the confined optical modes.[34] We have developed such a phase-sensitive setup with a scattering-type SNOM (s-SNOM), also called apertureless SNOM (see Fig. 5).

The s-SNOM technique uses a bulk atomic force microscope (AFM) probe as a nanoantenna instead of a near-field optical fiber probe. The field locally scattered by the dielectric or metallic tip apex is then collected by a classical microscope objective. This technique was first proposed by Boccara[35] and by Wickramasinghe and Williams[36] at the end of the 1980s but was merely ignored during a long time for the characterization of optical waveguides. There are, however, several motivations for the development of this alternative near-field microscopy:

(i) Commercially available AFM tips are sharp, robust, and very reproducible. They provide an increased topographic resolution as well as a better optical resolution, if we assume that they are both given by the tip apex diameter.

(ii) Scattering occurs at any wavelength. It is thus possible to work with the same kind of probe from the visible range

to the terahertz range, whereas near-field fiber probes would encounter transmission problems. The main restriction is that the scattering cross section must be high enough in order to get a sufficient signal-to-noise ratio.

(iii) The polarized field scattered by the probe in a given direction can provide information about the local-field polarization. This analysis task is rather simple when the tip can be considered as a dipole emitter (such as a small dielectric sphere above a low reflecting waveguide surface).

The main drawback of the s-SNOM over the coated fiber probe SNOM is probably its sensitivity to the radiation losses. In addition to the tip scattered field, the scattering losses in the collection zone are also collected, leading to an intrinsic interferometric signal.[37] It has been previously shown that the radiation losses cannot be suppressed by only modulating the tip in tapping mode and by using a lock-in detection at the tip vibration frequency f (see the Appendix). However, using a heterodyne detection scheme, the radiation losses effect can be canceled as proposed by Keilmann and co-workers.[38,39] This can be achieved by using the Mach-Zehnder interferometer shown in Fig. 5, and a lock-in detection working at the frequency $f \pm \Delta F$, with ΔF the frequency shift induced by the acousto-optic modulator.

B. s-SNOM setup and signal

The general experimental setup used in this study is shown in Fig. 5. It is based on the combination of an atomic force microscope and a confocal microscope in a Mach-Zehnder configuration. Light is injected in the device under study *via* a polarization controller. The AFM tip oscillating in intermittent contact at its own resonance frequency f is kept at a typical amplitude A of a few tens of nanometers equal to the average probe altitude $\bar{z}$. A part of the guided mode energy is hence periodically converted in radiation modes and the light scattered by the tip is collected by a confocal microscope.

We denote this collected field as $\mathbf{E}_p$. In order to achieve a symmetric detection, the detection direction is perpendicular to the propagation direction of the two guided modes. We then assume that the small AFM probe is passive and that $|\mathbf{E}_p(x,y,z)|$ is proportional to the local-field amplitude at the probe position $|\mathbf{E}(x,y,z)|$.

For devices having non-negligible optical scattering losses, we may have to consider a second collected field $\mathbf{E}_d$ related to the radiation losses in the confocal zone ($25\text{-}\mu\text{m}^2$ surface). Finally the total collected electric field is multiplexed with a reference field $\mathbf{E}_{ref}$ that is frequency shifted by ΔF.

Using this heterodyne interferometric detection, it becomes possible to cancel the radiation losses' effect, by using a lock-in amplifier working at the frequency $\Delta F - nf$ (for a better reading details are given in the Appendix, more information can also be found in Ref. 40). For these demodulation frequencies, the amplitude and the phase outputs R and Θ give, respectively, the amplitude and phase of the local field. For example, in the case of a single guided mode with a transverse optical constant γ, we have (cf. the Appendix)
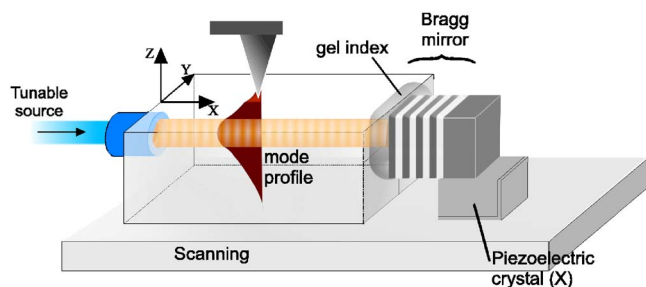
FIG. 6. (Color online) Experimental setup for the effective length measurement. Light coming from a tunable optical source is injected in a low loss ion exchanged waveguide with an input optical fiber. Both the input fiber and the sample are scanned. A part of the optical near-field related to the guided modes is diffracted by the probe before the grating and is far-field detected with a confocal type microscope (not shown here).

$$\begin{cases} R_{\Delta F \pm nf} \propto E_p^o e^{-|\gamma|\bar{z}} \propto E(x,y,\bar{z}) \\ \Theta_{\Delta F \pm nf} = \phi_p + cte \end{cases}, \quad (15)$$

where ϕ_p is the phase of the complex field $\mathbf{E}_p$ related to the probe and E_p^o is the amplitude of $\mathbf{E}_p$ at the surface. If the total collected field is not multiplexed (without Mach-Zehnder interferometer), the lock-in amplifier at the tip frequency f or harmonics nf will give an amplitude signal

$$R_{nf}(x,y,\bar{z}) = ||E_p^o|^2 e^{-2|\gamma|\bar{z}} I_n(2A|\gamma|) + 2|\mathbf{E_p^o}\mathbf{E_d}|\cos(\Delta\phi_{pd})e^{-z_0|\gamma|} I_n(|\gamma|A)|, \quad (16)$$

where the second term is an interferometric homodyne term between the optical radiation losses and the field scattered by the probe. I_n are the modified Bessel functions of the first kinds that are constants during the scans ($A=cte$). In the following we call this recorded signal R_{nf}, intensity images. The signal R_{nf} actually corresponds to the local intensity if the scattering losses are weak. As described in the Appendix and in Ref. [21,37], and [41], if the collected scattering losses E_d are not small, the s-SNOM images $R_{nf}(x,y,\bar{z})$ exhibit recog-

nizable oblique fringes that can be used (cf. Sec. IV B 2) or filtered out in order to obtain the intensity image.

IV. EXPERIMENTAL RESULTS

A. Intensity mapping: Effective length and displacement measurement

We first consider the case of a constant effective length. This kind of measurement has already been demonstrated in the case of a simple interface by Vander Rhodes *et al.*[42] in 1999 using an aperture SNOM. As a preliminary study to the variable effective length case, we report here the same kind of experiment but performed with a s-SNOM and in the case of a mobile Bragg mirror.

Figure 6 shows the experimental setup allowing determination of the effective length l_{eff}. A constant power (10 mW) tunable laser source (OSICS-ECL1560) is coupled in a pigtailed single-mode ion exchanged waveguide exhibiting very low dispersion. On the exit facet, an index matching gel cancels the Fresnel reflection. The multilayer is then brought very close to the waveguide. This mirror is mounted on a piezoelectric crystal in order to adjust precisely its position and hence l_{eff}. Details about this kind of mirror can be found in Ref. [43]; we just mention here that this mirror has a very wide stop band (1400–1600 nm) centered slightly below 1500 nm. The probe is put at a macroscopic distance from the Bragg structure and the waveguide center is scanned under the tip on a 10-μm distance.

Figure 7 shows the s-SNOM signal recorded for increasing wavelength within the reflection band, where the effective length is known to be constant. As the wavelength increases, a quasilinear variation of the phase shift $\Delta\phi_x$ is observed. The standing waves contrast remains the same showing that the LCR amplitude does not vary, on the plateau. Figure 7(b) shows the phase evolution of the LCR as a function of the wavelength. This phase spectrum was plotted with the measured values of $\arg[F_I(2\beta x)]$ on each FT of the profiles.
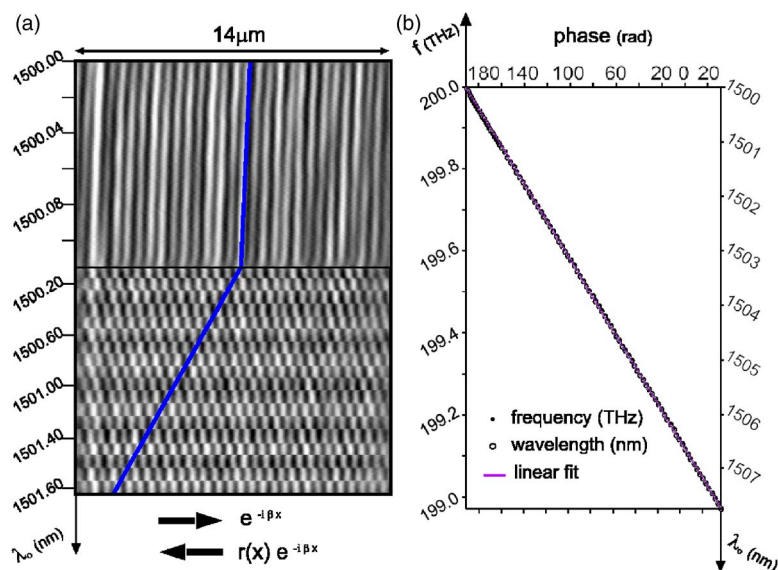
As stated previously, the conditions

FIG. 7. (Color online) Measure of a constant effective distance: (a) s-SNOM profiles $R_f(x,\lambda_0)$ of standing waves recorded along the single-mode waveguide for several wavelengths (first fine, then coarse tuning). The vacuum wavelengths λ_0 are fixed by a tunable source. An isophase shift line is drawn to show the shift direction of the standing waves. (b) Phase shift $\Delta\phi_x$ measured in the center of the s-SNOM profile by Fourier analysis.
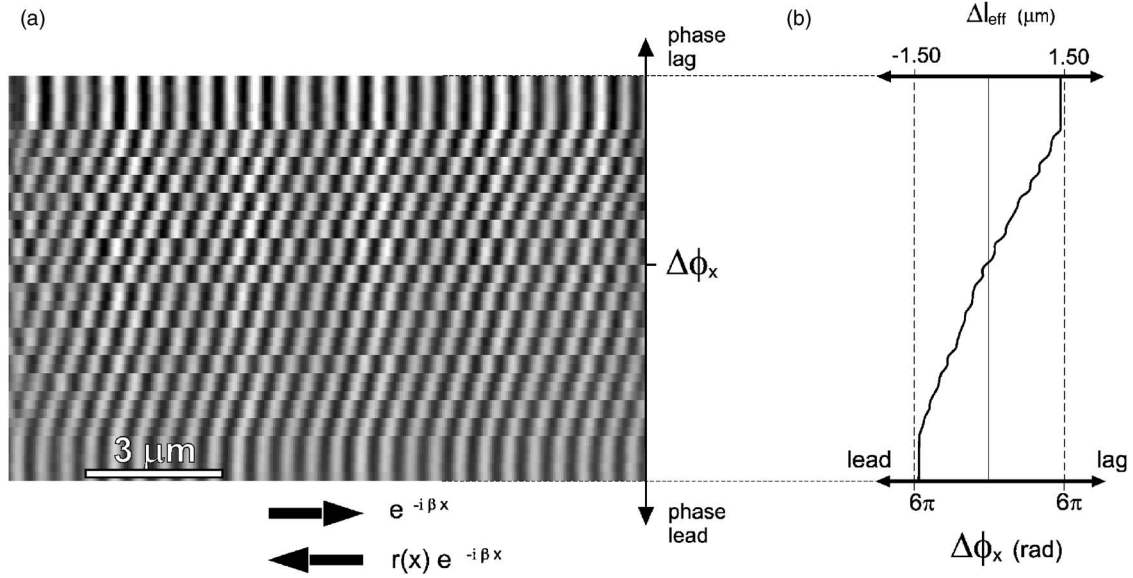
FIG. 8. Displacement measurement. (a) s-SNOM profiles recorded along a single-mode waveguide located before a mobile mirror. The visible variation of $\Delta\phi_x$ is the result of a controlled mirror displacement. (b) Variation of the LCR phase recorded on the phase of the FT profiles and related displacement.

$$\frac{dl_{eff}}{d\sigma} \approx 0 \quad \text{and} \quad \frac{d\beta}{d\sigma} \approx 0 \qquad (17)$$

are fulfilled in the short-wavelength range of the measured spectrum (1500–1508 nm). Following Eq. (6), l_{eff} can be expressed with the slope of the phase spectrum as

$$l_{eff} = \frac{1}{4\pi n_{eff}} * \frac{d\Delta\phi}{d\sigma} = \frac{\lambda\lambda'}{4\pi} \frac{(\Delta\phi_x' - \Delta\phi_x)}{\lambda' - \lambda},$$

where the effective index $n_{eff} = \beta/(2\pi\sigma)$ connects the vacuum wavelengths (λ_0) with the measured wavelengths ($\lambda = \lambda_0/n_{eff}$). Experimentally, the measured effective distance is $l_{eff} = 3.600$ mm± 15 μm. The obtained precision could be, however, improved by increasing the wavelengths range or by getting closer to the mirror.

Another direct application of the LCR phase retrieval is the measure of effective length variations, i.e., the measure of displacements. Figure 8 illustrates how from the standing-wave pattern shift, the displacement can be directly recorded with a high precision. To observe a displacement, the previous Bragg mirror was slightly moved with the piezoelectric system at a fixed wavelength. The displacement measurement is then obtained by reading the LCR phase of the profiles. We can note that the measurement of a profile takes in our case a minimum time of 0.2 sec limited by the tapping mode feedback. The measurement speed could be increased, for example, by working in constant height, probably up to more than 50 Hz, which may still be seen as slow for a number of applications. However, real time measurement can be easily obtained by stopping the raster scanning and reading the temporal variation of the optical signal $|E_p|$ as the mirror is moving (without imaging).

B. Intensity mapping: LCR retrieval

For a Bragg grating structure with an arbitral complex response, the effective length as well as the amplitude of the LCR may strongly vary with the wavelength. Both phase and amplitude of the LCR can be retrieved using the near-field intensity images given by R_f or $R_{\Delta F-f}^2$ with the method presented in Sec. II B. Recently, we have reported on the LCR retrieval of two single-mode Bragg gratings structures[20,21] consisting in a corrugated ion exchanged waveguide and a fiber Bragg grating. In this part, we will comment further on the obtained results as well as on the normalization procedure. We also present the LCR of another ion exchanged waveguide revealing the presence of leaky modes.

1. Example of LCR spectrum: Weak grating

The first device under study was a single-mode ion exchanged waveguide in glass, on which a $\Lambda = 500$-nm pitch grating was slightly etched by reactive ion etching. The diffused waveguide core is rather symmetric enabling a good coupling with the injection fiber and has a slightly higher refractive index ($\Delta n = 10^{-3}$). Some details on this kind of Bragg grating structures can be found in Ref. 44.

Figure 9(a) shows an experimental standing-wave spectrum recorded on the waveguide surface, before the weak grating corrugation. These standing-wave profiles were obtained by mapping the intensity along the same scanning line for different wavelengths near the Bragg resonance. On the recorded profiles $R_f(x, y = cte, \bar{z} = cte)$ we can clearly observe a modification of both the phase shift and the intensity as a function of the wavelength. Note that the homodyne interferometric contribution in R_f, corresponding to the second term in Eq. (16), can be clearly distinguished in a Fourier analysis (cf. the following Sec. IV B 2 or the Appendix) and has been filtered out for clarity.
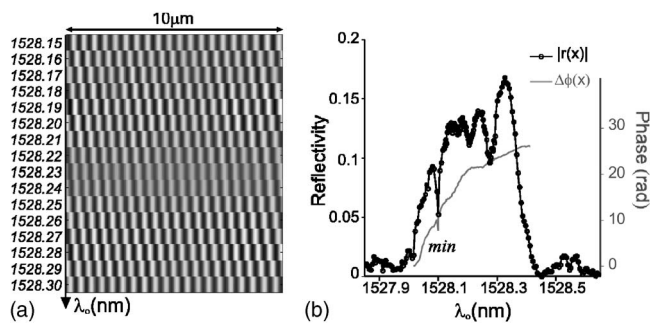
FIG. 9. (a) Experimental s-SNOM image of a standing-wave spectrum recorded on a buried waveguide with a weak corrugation, before the grating. The sample is scanned along the x direction (y, and $\bar{z}$ constant) and the wavelength is increased between each line. Sixteen scanning lines corresponding to 16 different wavelengths are represented. (b) Amplitude and phase of the LCR extracted from a full SWS. The phase of the LCR measured is measured at the center of the scan.

Following the method based on intensity mapping, the LCR spectrum was extracted from the experimental standing-wave spectra. Figure 9(b) shows the LCR spectrum of the grating near the Bragg wavelength. The two spectra were obtained by plotting for each wavelength (i.e., for each scanning line) the amplitude and the phase of the Fourier transform at the standing-wave spatial frequency.

For this grating, the reflection is very weak and is even difficult to observe in far field. Some defects in the grating entail minima in the amplitude resonance and we can note that the strong minimum noted *min* corresponds with a fast phase variation. In the case of such a weak reflection, the need of a high optical resolution is not too critical (see Fig. 4) for the absolute LCR amplitude retrieval, so that it can be derived from the SWS contrast. However, as mentioned in Refs. 20 and 21, the absolute value of the LCR can also be retrieved experimentally from the interferometric term contribution in the s-SNOM intensity signal $R_f(x,y)$. This method, which is specific to the s-SNOM working in intensity mode, allows one to recover the absolute value of the LCR amplitude without the penalty inflicted by a limited optical resolution. This normalization procedure is described below.

2. s-SNOM normalization procedure

Figure 10(a) shows an intensity image $R_f(x,y)$ of the standing wave recorded near the resonance wavelength (λ_0 =1528.270 nm). The image was recorded willingly in a lossy zone (close to optical radiation losses). In such zone where non-negligible scattering occurs ($\mathbf{E}_p \gtrsim \mathbf{E}_d$), typical tilted fringes can be observed in addition to the standing waves, despite the fact that the intensity term related to $\mathbf{E}_d$ is not present in the $R_f(x,y)$ signal. As shown by Fig. 10(b), the fringes are also visible as spots on the two-dimensional (2D) Fourier transform of the s-SNOM image. A detailed description of this effect with several experimental examples can be found elsewhere.[37] We can, however, emphasize that these tilted fringes do not correspond to the real *local* intensity distribution: the scattering losses in the small collection zone
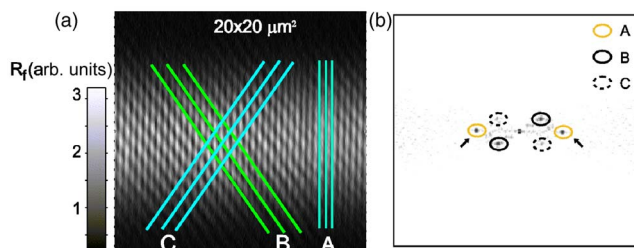

FIG. 10. (Color online) (a) s-SNOM image recorded at tip frequency before an ion exchanged Bragg grating waveguide, near the resonance (1528.270 nm). Three fringe patterns are visible: the standing-wave pattern and two oblique fringe patterns induced by the scattering losses and the two guided modes (β and $-\beta$). (b) 2D spatial Fourier transform of the s-SNOM image.

are usually stemming from several distributed sources (point scatterers, roughness) and would not present such a clear structure in the near field. On the opposite, the peculiar structure of both figures [Fig. 10(a) and 10(b)] entails that the $\mathbf{E}_d$ field has a completely specified k-space structure.

The tilted fringes apparent here are actually given by the homodyne term of interference between the two fields detected in *far field* $\mathbf{E}_p$ and $\mathbf{E}_d$ [and more precisely by their phase relation $\Delta\phi_{pd}$ in Eq. (16), whose expression is given in the Appendix as a function of the sample position]. The phase variation from $\mathbf{E}_d$ during a scan has a simple expression because all the scatterers contributions, within the diffraction-limited collection area, are merged by the confocal optical system in a single equivalent one along the Y direction. The second phase term (from $\mathbf{E}_p$), given by the fixed tip during the sample scan, varies according to the guided mode directions (X). Here, two symmetrical tilted fringes are apparent due to the contribution of both reflected and impinging mode (along $\pm X$). In other words, the direction and the periodicity of the fringes can be foreseen from the guided modes propagation directions and the detection direction (for an experimental demonstration, see, for example, Fig. 4 from Aubert *et al.*[37]).

Let us now see how to normalize the LCR spectra from this natural interferometric behavior. The analytical expression of the 2D Fourier transform of the s-SNOM signal is here given by

$$F(f_x,f_y) = \mathcal{F}(R_f(x,y,A)) = F_A(f_x) + F_B(f_x,f_y) + F_C(f_x,f_y),$$
(18)

with

$$F_A(f_x) = I_n(2A|\gamma|)|E_p^{o+}|^2 * \{[1 + |r(x)|]\delta(f_x) + |r(x)|$$
$$* [e^{-i2\beta x_{eff}}\delta(f_x - 2\beta_x) + e^{i2\beta x_{eff}}\delta(f_x + 2\beta_x)]\},$$

$$F_B(f_x,f_y) = I_n(A|\gamma|)2|E_p^{o+}||E_d| * [e^{-i\Delta\Phi_1}\delta(f_x + f_y - \beta_x + k_d)$$
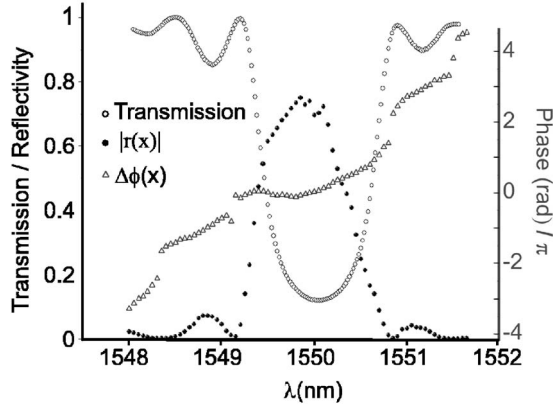$$+ e^{i\Delta\Phi_1}\delta(f_x + f_y + \beta_x - k_d)],$$

FIG. 11. Normalized complex reflectivity of a fiber Bragg grating obtained by standing-wave imaging compared with far-field transmission.

$$F_C(f_x,f_y) = I_n(A|\gamma|)2|E_p^{o-}||E_d| * [e^{-i\Delta\Phi_2}\delta(f_x + f_y - \beta_x - k_d)$$
$$+ e^{i\Delta\Phi_2}\delta(f_x + f_y + \beta_x + k_d)],$$

where A is the tip oscillation amplitude here equal to $\bar{z}$, $E_p^{o\pm}$ are the detected complex fields related to the forward and reflected guided modes, and $\Delta\Phi_1$ and $\Delta\Phi_2$ are the phase shifts between these two fields and the reference field. The peaks corresponding to the three terms are pointed out on the Fourier transform of the image [Fig. 10(b)]. In the term F_A, $F(\pm 2\beta_x, 0)$ is related to the standing wave whereas the terms $F_B = F(\pm\beta_x, \mp k_d)$ and $F_C = F(\pm\beta_x, \pm k_d)$ are related to the interferences between the losses and the two guided modes. The reflection coefficient at a given wavelength can then be estimated from the ratio of the two peaks (B) and (C):[51]

$$\left|\frac{F_C(f_x,f_y)}{F_B(f_x,f_y)}\right| = \left|\frac{E_p^{o-}}{E_p^{o+}}\right| = |r(x)|. \quad (19)$$

This method is very interesting to estimate the absolute value of $|r(x)|$ since thanks to the phase information given by the two homodyne terms (B and C) the two fields can be clearly discriminated on the 2D FT. Compared with the value given by the contrast, this method takes advantage of the intrinsic nonlocal interference between the radiation losses and the two guided modes contributions from opposite directions and is hence not limited by the tip size (resolution).

3. Example of LCR spectrum: Fiber Bragg grating

The LCR retrieval method was also applied to a commercial single-mode fiber Bragg grating whose spectral characteristic was well known. This device consists in a periodic modulation of the index of refraction along the fiber core. This fiber was chemically thinned in order to enable the scattering of the exponentially decaying field close to the core and hence the standing wave to be imaged.

Figure 11 shows the recovered LCR spectrum (phase and amplitude) compared with a far-field measurement. The measured far-field transmission is found in agreement with the *in situ* reflectivity spectrum. In this case, the standing-wave pattern was registered at the beginning of the apodized grating. The phase variation of the measured LCR is hence ex-

pected to be very similar to the phase shift induced by the sole grating without additional propagation. However, the phase shift variation entailed by a standard periodic Bragg grating is known to be monotonic within the resonance with a total variation of 2π from one minima to the other [e.g., Fig. 1(c)]. We believe that the observed differences mainly arise from mechanical instability and slight thermal drift that spectrally shift the resonance peak during the acquisition. The mechanical drift of the thinned fiber and/or the scanning stage can also explain the nonmonotonic variation of the phase. The small discrepancies observed could also be attributed to a sensitivity to leaky modes that are not considered in this analysis.

4. Example of LCR: Leaky modes structure

In a waveguiding structure because of perturbations such as for example a bend, a grating or a defect, a part of the guided mode energy will be coupled out in other (discrete) guided modes or in the continuum of radiation modes. By definition, the radiation modes are not confined in at least one direction perpendicular to the waveguide and are hence negligible after a given propagation distance. But in some cases, groups of radiation modes fulfill the transverse resonance condition and have to be considered on large distance to correctly account for transient state propagation. For a good physical understanding of the field propagation in the real space, "leaky modes" representation can then be used to model the effect of the resonances in the radiation spectrum.[45]

Unlike optical fibers, the waveguides are usually asymmetric and the radiation mode groups are often called "semi-leaky modes" because some radiation modes are selectively confined in one direction while slowly radiating in another one. This can be for example the case for a ridge[46] or a surface waveguide. Now, if a grating is etched on such a leaky mode structure, reflectivity spectra measured locally may exhibit unexpected discrete resonances. Moreover, these resonances are generally not visible in a standard reflection measurement because the leaky modes are not efficiently coupled back in the injection fiber, or do not reach the far-field detection.

Figure 12(a) shows the local reflectivity spectra amplitude of such a structure. Several resonances are visible. In this case, the Bragg grating was deeply etched (450 nm) on a single-mode surface waveguide obtained by K^+/Na^+ ion exchange on a doped glass substrate (some details can be found in Ref. 44). This kind of waveguide usually presents a rather symmetric core enabling a good coupling with optical fiber. However, in this case, due to a specific process, the zone above the highly exchanged region presents a strong dip in the topography and hence a stronger confinement in the vertical direction. Figure 13 shows the topography of the waveguide before the grating and a simultaneously recorded s-SNOM image at the Bragg resonance. Due to this characteristic topography, the equivalent slab waveguide along the vertical direction would present several guided modes, but these modes are actually leaking due to the weak confinement along the horizontal direction.
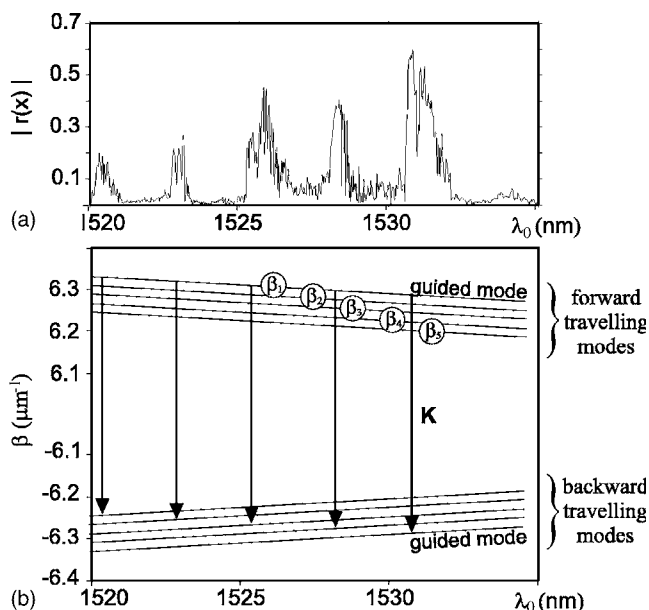
FIG. 12. (a) Reflectivity spectrum of a dissymmetric single-mode waveguide. Despite the single-mode character of the low dispersion waveguide, several maxima are visible. (b) Ewald diagram corresponding to the LCR spectrum.

The different maxima observed on the LCR spectrum (Fig. 12) can hence be explained by a coupling between the guided mode and the leaky modes. Therefore the average optical constants of the radiation modes groups corresponding to the leaky modes can be retrieved with an Ewald construction for each resonance.[46] According to the Bragg law, the grating creates a coupling between two modes n and m if the difference of their optical propagation constant is equal to the grating vector $K=2\pi/\Lambda$:

$$\beta_n(\lambda) - \beta_m(\lambda) = \frac{2\pi}{\Lambda}. \tag{20}$$

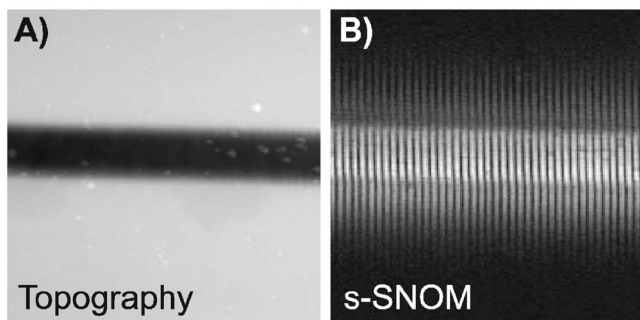For the two (back and forth) guided modes this relation is simply expressed by

FIG. 13. Topography (A) and optical image (B) of an ion exchanged waveguide (leaky mode structure). The optical image was here recorded at the Bragg resonance with the interferometric heterodyne setup (no tilted fringes are visible).

$$\beta_1(\lambda) - \beta_{-1}(\lambda) = \frac{2\pi}{\Lambda}. \tag{21}$$

In order to plot the dipersion of these optical constants, they can be expressed as a function of the vacuum wavelength λ_0 as

$$|\beta_{\pm 1}(\lambda_0)| = \pm n_{eff\,1}\frac{2\pi}{\lambda_0}, \tag{22}$$

where the effective index $n_{eff1}=\lambda/\lambda_0$ can be obtained from the measured periodicity of the standing wave $\lambda/2$. The dispersion of $\beta_1(\lambda_0)$ is plotted in Fig. 12, assuming that the measured effective index is constant within the LCR spectrum.[52] The propagation constant of higher modes such as leaky modes being smaller than β_1, the coupling occurs for smaller wavelengths. The corresponding Ewald diagram allowing retrieval the optical constants is given in Fig. 12.

C. Complex field maps: Heterodyne detection

1. Introduction

The s-SNOM signals R and Θ given by the lock-in amplifier working at $\Delta F \pm nf$ directly give the amplitude and the phase of the detected field scattered by the tip $\mathbf{E}_p$. As mentioned in the theoretical part, the complex field mapping presents several advantages for the determination of the complex responses of photonic structures. The Fourier analysis of the complex field enables a direct modal analysis and therefore allows one to determine the LCR of several guided modes separately. In the other hand the Fourier analysis of the amplitude or intensity $|\mathbf{E}_p|^2$ only is more difficult to interpret when dealing with multimode devices. We will not focus in this paper on this point. An example of direct modal analysis with the heterodyne s-SNOM performed on a multimode planar waveguide can be found elsewhere.[47] Moreover, complex fields can also be recorded in transmission as well as in reflection in order to retrieve both group delays τ_{refl} and τ_{transm}, which is not possible with the only amplitude information.

An example of complex field mapping obtained with this setup is shown in Fig. 14. In addition to the phase retrieval, the usual contribution of the radiation losses is canceled, so that no tilted fringes are visible on the image. This last point is naturally important because this "background" field $\mathbf{E}_d$ is not controlled and would hide the real near-field signal corresponding to the tip $\mathbf{E}_p$ if the ratio $\mathbf{E}_p/\mathbf{E}_d$ is too weak.

However, in the previous section on intensity mapping, we have shown that the interferences between the two collected fields $\mathbf{E}_d$ and $\mathbf{E}_p$ can be useful. The homodyne interferometric terms in R_f produce recognizable fringes that can be used to discriminate the modes guided in opposite directions and thus to obtain the absolute value of the reflection coefficient of the Bragg grating structures. This specific information is naturally lost in the complex field mapping at $\Delta F \pm nf$ but the complex field mapping is supposed to be less sensitive to the probe averaging for the LCR determination. Hence the obtained error on the LCR value can still be considered small at telecommunications wavelengths if the AFM tip is reasonably small (see Fig. 4).
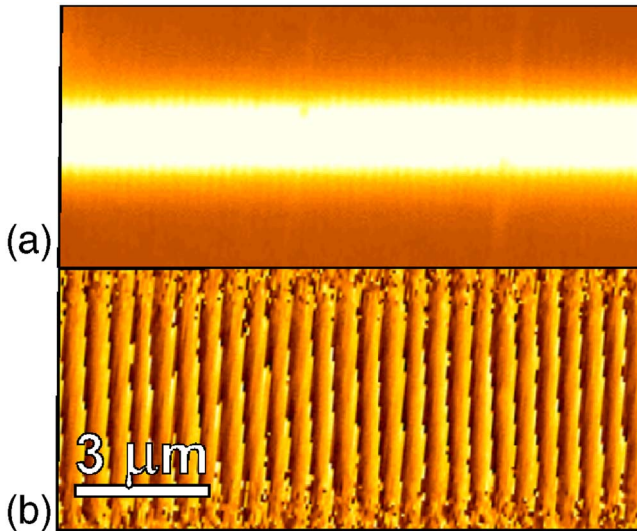
FIG. 14. (Color online) Example of s-SNOM complex field mapping obtained on an ion exchanged waveguide in the case of a weak reflection. (a) Amplitude of the local field $R_{f-\Delta F}(x,y)$. (b) Phase of the local field $\Theta_{f-\Delta F}(x,y)$.

A review of all the advantages of phase sensitive s-SNOM is given elsewhere.[40] In the following section, we will give experimental results obtained with a phase sensitive s-SNOM on the LCR determination.

2. Complex field profiles before a grating

Using the heterodyne s-SNOM, the amplitude and the phase of the complex field were recorded on an ion exchanged waveguide prior to the grating. Figure 15 shows several complex field profiles. The reflection was continuously increased by tuning the wavelength near the Bragg resonance. Experimental results are found to be in good agreement with the expression of $\Phi(x)$ [Eq. (13)].

The Fourier transform magnitude of each windowed complex profile is shown in Fig. 16. The forward and the reflected guided mode appear as two separated peaks. The value of $r(x)$ is simply given by the ratio of the two peaks and as mentioned previously is less dependent on the optical resolution than a direct measure of the contrast on the amplitude image.

Both complex transmissivity and reflectivity spectra of photonic structures are currently investigated using the heterodyne s-SNOM.

V. CONCLUSIONS

In conclusion, LCR retrieval methods based on standing-wave imaging have been both theoretically and experimentally investigated. The methods are based on the intensity or complex field mapping of standing-wave profiles using a SNOM and a highly coherent tunable optical source. Experimentally, the LCR was determined using a simple Fourier analysis of the standing-wave spectrum obtained with an s-SNOM.

The main motivation for the s-SNOM approach is the small size of the scattering probe, which is needed for a good
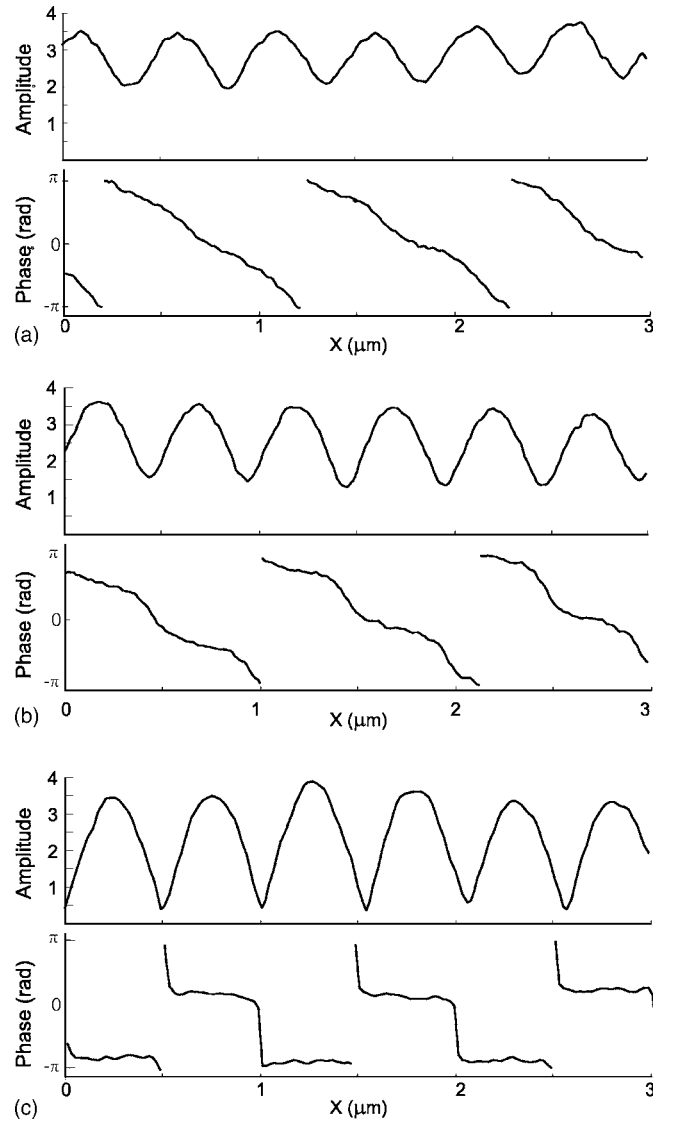

FIG. 15. Complex field profiles recorded prior to a Bragg grating for increasing reflection coefficients: (a) below the resonance ($\lambda_0 = 1530.60$ nm), (b) close to the resonance ($\lambda_0 = 1530.66$ nm), and (c) at the resonance ($\lambda_0 = 1530.77$ nm). The amplitude signal is given in arbitrary units.

precision on the LCR determination. In intensity mode, a limitation of the s-SNOM technique arises from the radiation losses in the collection zone that nonlocally interfere with the field related to the probe. Nevertheless, information can be extracted from this interferometric behavior. Beside the losses localization, this effect allowed us to retrieve the local absolute coefficient.

The technique presented here has been applied to several Bragg grating waveguides but can also be directly applied in front of photonic crystals or hybrid structures such as active waveguide coupled with an external DBR allowing then an *in situ* determination of the coupling losses.

Furthermore, the phase-sensitive s-SNOM we have developed based on a heterodyne detection allowed us to cancel the effect of background light not modulated by the local probe. Numerous advantages are given by this improved
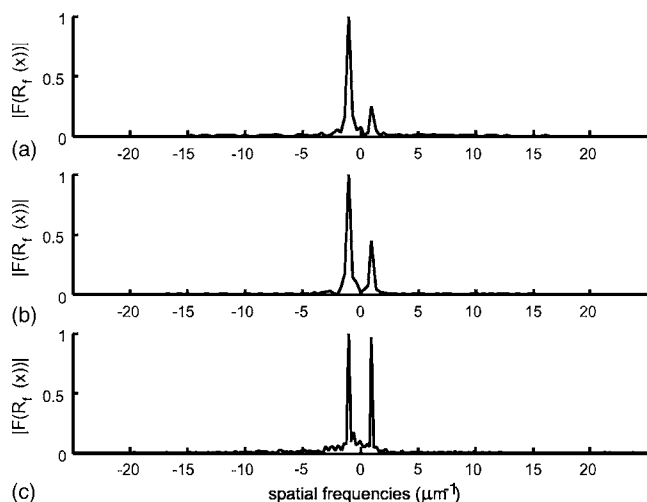
FIG. 16. Fourier transform amplitudes of the complex profiles given in Fig. 15 (arbitrary units).

setup such as simplified modal analysis or signal amplification.

In addition to the optical signature in reflection, the complex signature in transmission can also be determined from the complex field mapping provided by the developed microscope. The combination of both measures would give the transfer matrix of individual micro- and nanodevices as a function of the wavelength. Moreover, given the natural sensitivity of the s-SNOM to the local-field polarization, cross-reflection coefficients between TE and TM modes could also be obtained.

APPENDIX: S-SNOM SIGNAL FOR GUIDED MODES

In the setup shown in Fig. 5, three important detected fields can be considered. These are the field related to the probe sample interaction $\mathbf{E}_p$, the field related to the scattering losses $\mathbf{E}_d$, and the reference field $\mathbf{E}_{ref}$, which is frequency shifted by ΔF with the acousto-optic modulators. The phase of these fields are, respectively, noted ϕ_p, ϕ_d, and ϕ_{ref}. The total electric field collected by the objective plus the reference field is

$$\mathbf{E}_{det} = \mathbf{E}_p e^{\mathbf{i}\phi_p} + \mathbf{E}_d e^{\mathbf{i}\phi_d} + \mathbf{E}_{ref} e^{\mathbf{i}\phi_{ref}}. \quad (A1)$$

$\mathbf{E}_{ref}$ can be considered as a constant amplitude field whereas $\mathbf{E}_p$ depends on the (x,y) position of the probe on the sample (at $z=0$), and on the average altitude of the AFM tip $\bar{z}$. The field related to the radiation losses $\mathbf{E}_d$ is supposed not to be modulated by the probe (i.e., independent from the tip height modulation).

To derive the s-SNOM signal in the case of optical confined modes, we will first express the signal related to the probe $\mathbf{E}_p$ (signal for $\mathbf{E}_d$ and $\mathbf{E}_{ref}$ equal to zero), then we will consider the homodyne case ($\mathbf{E}_{ref}=0$), and finally the heterodyne case.

1. Field scattered by the probe and related signal

In this section, we express the detected signal related to $\mathbf{E}_p$ the field scattered by an oscillating probe. This derivation can be found in Refs. 37 and 48. First, we assume that the field scattered by the probe at the (x,y,z) position above the x-invariant waveguide is proportional to the local field $\mathbf{E}(x,y,z)$ without the probe (weak-coupling regime[49]). Hence $\mathbf{E}_p$ can be written

$$\mathbf{E}_p(x,y,z) = \mathbf{E}_p^o e^{\mathbf{i}\gamma z} \quad \text{with} \quad \mathbf{E}_p^o = \mathbf{E}_p(x,y,0), \quad (A2)$$

where γ is the imaginary transverse optical constant of a guided mode, related to the effective index n_{eff} by $\gamma = \sqrt{\frac{4\pi^2}{\lambda_0^2} - \beta^2}$ with $\beta = n_{eff} 2\pi/\lambda_0$.

In tapping mode the tip oscillates with an amplitude A and a frequency f. The altitude z in Eq. (A2) is then given by $z(t) = \bar{z} + A \cos(2\pi ft)$. When the tip scans the surface the amplitude A becomes equal to $\bar{z}$, and A is equal to the free amplitude A_l when $\bar{z} > A_l$.

Since the lock-in detection can extract the different harmonics (f, $2f$, $3f$,...) of the detected signal, it is useful to develop $\mathbf{E}_p$ in Fourier series:

$$\mathbf{E}_p = E_p^o e^{-|\gamma|[\bar{z}+A\cos(\Omega t)]} e^{\mathbf{i}\phi_p} \mathbf{u}_p = E_p^o e^{-|\gamma|\bar{z}} e^{\mathbf{i}\phi_p} \mathbf{u}_p \sum_{n\in\mathbb{Z}} I_n(|\gamma|A) e^{\mathbf{i}n\Omega t},$$
$$(A3)$$

with $\Omega = 2\pi f$ and I_n the modified Bessel functions of the first kind.

Hence in the simplest case where the field $\mathbf{E}_p$ is only detected, the amplitude output of the lock-in amplifier demodulating at the nf frequency is given by

$$R_{nf}(x,y,\bar{z}) = ||E_p^o|^2 e^{-2|\gamma|\bar{z}} I_n(2A|\gamma|)|, \quad (A4)$$

where in tapping mode ($A=cte$), $I_n(2A|\gamma|)$ is constant.

2. Homodyne signal

When the scattering losses collected by the objective given by $\mathbf{E}_d$ are non-negligible compared to $\mathbf{E}_p$, the field collected by the microscope becomes

$$\mathbf{E}_{det} = \mathbf{E}_p e^{\mathbf{i}\phi_p} + \mathbf{E}_d e^{\mathbf{i}\phi_d}. \quad (A5)$$

The reference field being set to zero, both fields will interfere on the detector resulting in a homodyne interference:

$$I(x,y,\bar{z})_{det}^{hom} = |\mathbf{E}_p|^2 + 2|\mathbf{E}_d \mathbf{E}_p| \cos(\Delta\phi_{dp}) + |\mathbf{E}_d|^2, \quad (A6)$$

with $\Delta\phi_{dp} = \phi_p - \phi_d$. One can emphasize that the intensity term $|\mathbf{E}_d(x,y)|^2$ related to the radiation losses, does not depend on the tip altitude and is hence not detected by the

lock-in amplifier working at the tip frequency f or higher harmonics. However the interferometric term, which is modulated at the tip frequency is not suppressed by the lock-in amplifier. From Eq. (A3), we can find the terms of the Fourier series of Eq. (A6), which are given by the amplitude signal of the lock-in amplifier demodulating at the nf frequencies:

$$R_{nf}(x,y,\bar{z}) = \left| |E_p^o|^2 e^{-2|\gamma||\bar{z}|} I_n(2A|\gamma|) \right.$$
$$\left. + 2|\mathbf{E}_p^o \mathbf{E}_d| \cos(\Delta\phi_{dp}) e^{-z_0|\gamma|} I_n(|\gamma|A) \right|. \quad \text{(A7)}$$

In addition to the intensity signal related to the probe, a homodyne interferometric term is detected. The local phase variation of the field scattered by the tip is hence converted in an amplitude modulation. As we will see later, this allows us to distinguish between guided modes propagating in different directions and especially in opposite directions. Actually, the interferometric term in Eq. (A7) corresponds to the oblique fringes observed in the experimental images. This has been detailed in Refs. 37 and 41 and is briefly discussed hereafter.

Let us express $\Delta\phi_{dp}$ as a function of the probe position (x,y) in the sample plane $(\mathbf{X}, \mathbf{Y})$. This phase shift is the phase difference between the collected fields $\mathbf{E}_d$ and $\mathbf{E}_p$. The phases of both fields change on the detector as the sample is scanned. On one hand, the radiation losses sources in the collecting zone (a small dust for example) follow the sample movement. For example, the optical path of $\mathbf{E}_d$ in the air increases if the sample is scanned away from the collecting objective. The phase variation of $\mathbf{E}_d$ during the scan in the (X, Y) sample plane is $\mathbf{k}_d \cdot (x\mathbf{X} + y\mathbf{Y})$, where (x,y) is the tip position relatively to the sample and where $\mathbf{k}_d$ corresponds to the average wave vector of both collected fields $\mathbf{E}_d$ and $\mathbf{E}_p$ toward the microscope objective.

On the other hand, as the sample is scanned under the tip apex, the phase of the scattered field $\mathbf{E}_p$ changes according to the phase of the local propagating field. However, the distance between the tip and the objective remains constant. For a single guided mode β propagating along $\mathbf{u}_\beta$, the phase variation of $\mathbf{E}_p$ is hence $\beta\mathbf{u}_\beta \cdot (x\mathbf{X} + y\mathbf{Y})$.

Considering the two contributions, the phase shift is given by

$$\Delta\phi_{dp} = \beta\mathbf{u}_\beta \cdot (x\mathbf{X} + y\mathbf{Y}) - \mathbf{k}_d \cdot (x\mathbf{X} + y\mathbf{Y}). \quad \text{(A8)}$$

In our experimental conditions the field under study is guided along a $\mathbf{X}$ direction that is perpendicular to the detection direction $(\mathbf{Y})$. For a forward guided mode (along $+\mathbf{X}$) or a reflected guided mode (along $-\mathbf{X}$) the phase shifts reduce to

$$\Delta\phi_{dp}^\pm = \pm\beta x - \mathbf{k}_d y, \quad \text{(A9)}$$

yielding to two symmetrical fringes patterns on the optical image $R_{nf}(x,y)$. Further details about the s-SNOM signal in the case of a confined mode without reference field can be found elsewhere.[37]

3. Heterodyne signal

Considering now the three detected fields, the detected intensity is given by

$$I(x,y,\bar{z})_{det} = |\mathbf{E}_p|^2 + |\mathbf{E}_d|^2 + |\mathbf{E}_{ref}|^2 + 2|\mathbf{E}_d\mathbf{E}_p|\cos(\Delta\phi_{dp})$$
$$+ 2|\mathbf{E}_d\mathbf{E}_{ref}|\cos(\Delta\phi_{dr}) + 2|\mathbf{E}_p\mathbf{E}_{ref}|\cos(\Delta\phi_{pr}), \quad \text{(A10)}$$

with

$$\Delta\phi_{dp} = \phi_d - \phi_p,$$

$$\Delta\phi_{dr} = \phi_d - \phi_{ref} = \Delta\omega t + \phi_d + cte,$$

$$\Delta\phi_{pr} = \phi_p - \phi_{ref} = \Delta\omega t + \phi_p + cte, \quad \text{where } \Delta\omega = 2\pi\Delta F.$$

The two last terms in Eq. (A10) are heterodyne interferometric terms modulated at the beating frequency ΔF. One can already see that it is possible to selectively extract the last term since it is modulated at both the optical shift frequency ΔF and the tip oscillation frequency f. This is particulary interesting because this term does not depend on the radiation losses $\mathbf{E}_d$.

In order to explicit the s-SNOM signal corresponding to the detected intensity (A10), we can express the field related to the probe (A3) as

$$\mathbf{E}_p = E_p^o e^{-|\gamma||\bar{z}|} e^{i\phi_p} \mathbf{u}_p * \left(I_0(|\gamma|A) + 2\sum_{n\in\mathbb{N}^*} I_n(|\gamma|A)\cos(n\Omega t) \right). \quad \text{(A11)}$$

The detected intensity can then be written as

$$I(x,y,\bar{z})_{det} = I(x,y,\bar{z})_{det}^{hom} + I(x,y,\bar{z})_{det}^{het}, \quad \text{(A12)}$$

with

$$I(x,y,\bar{z})_{det}^{hom} = |\mathbf{E}_p|^2 + |\mathbf{E}_d|^2 + |\mathbf{E}_{ref}|^2 + 2|\mathbf{E}_d\mathbf{E}_p|\cos(\Delta\phi_{dp}),$$

$$I(x,y,\bar{z})_{det}^{het} = 2|\mathbf{E}_d\mathbf{E}_{ref}|\cos(\Delta\omega + \phi_d + cte) \quad \text{(a)}$$

$$+ 2E_p^o\mathbf{E}_{ref} \cdot \mathbf{u}_p e^{-|\gamma||\bar{z}|} I_0(|\gamma|A)\cos(\Delta\omega t + \phi_p + cte) \quad \text{(b)}$$

$$+ 2E_p^o\mathbf{E}_{ref} \cdot \mathbf{u}_p e^{-|\gamma||\bar{z}|} \sum_{n\in\mathbb{N}^*} I_n(|\gamma|A)$$
$$* \cos[(\Delta\omega + n\Omega)t + \phi_p + cte] \quad \text{(c)}$$

$$+ 2E_p^o\mathbf{E}_{ref} \cdot \mathbf{u}_p e^{-|\gamma||\bar{z}|} \sum_{n\in\mathbb{N}^*} I_n(|\gamma|A)$$
$$* \cos[(\Delta\omega - n\Omega)t + \phi_p + cte], \quad \text{(d)}$$

where $I(x,y,\bar{z})_{det}^{het}$ includes the intensity terms modulated at $\Delta\omega$. We can note that the homodyne signal $I(x,y,\bar{z})_{det}^{hom}$ is obviously very similar to the previous one. Let us consider now the heterodyne terms modulated at $\Delta\omega$ noted (a) and (b). If the signal from the probe is much higher than the signal related to the radiation losses, then (a) can be neglected. Then, the amplitude and phase outputs of the lock-in amplifier will give both the amplitude and the phase of the local field $E(x,y,\bar{z})$:

$$E_p^o \gg E_d \Rightarrow \begin{cases} R_{\Delta F} \propto E_p^o e^{-|\gamma|\bar{z}} \propto E(x,y,\bar{z}) \\ \Theta_{\Delta F} = \phi_p + cte \end{cases} . \quad (A13)$$

However, if the background field due to $\mathbf{E}_d$ is important, it is especially interesting to detect at the modulation frequencies

of the (c) or (d) terms. For these frequencies, even if the weight of $\mathbf{E}_d$ is important the lock-in amplifier outputs will directly give

$$\begin{cases} R_{\Delta F \pm nf} \propto E_p^o e^{-|\gamma|\bar{z}} \propto E(x,y,\bar{z}) \\ \Theta_{\Delta F \pm nf} = \phi_p + cte \end{cases} . \quad (A14)$$

[1] L. Poladian, Opt. Lett. **22**, 1571 (1997).
[2] S. Thibault, J. Lauzon, J.-F. Cliche, J. Martin, M. A. Duguay, and M. Tetu, Opt. Lett. **20**, 647 (1995).
[3] N. M. Litchinitser and D. B. Patterson, J. Lightwave Technol. **15**, 1323 (1997).
[4] S. Barcelos, M. N. Zervas, and R. Laming, Opt. Fiber Technol. **2**, 213 (1996).
[5] K. Ogawa, Y. Matsui, T. Itatani, and K. Ouchi, Appl. Phys. Lett. **12**, 155 (1998).
[6] A. Melloni, F. Morichetti, and M. Martinelli, Opt. Photonics News **14**(11), 44 (2003).
[7] H. Altug and J. Vuckovic, Appl. Phys. Lett. **86**, 111102 (2005).
[8] Y. Gottesman, E. V. K. Rao, D. Piot, E. Vergnol, and B. Dagens, Appl. Phys. B: Lasers Opt. **73**, 609 (2001).
[9] S. Ryu, Y. Horiuchi, and K. Mochizuki, J. Lightwave Technol. **7**, 1177 (1989).
[10] G. Genty, T. Niemi, and H. Ludvigsen, Opt. Commun. **204**, 119 (2002).
[11] A. Imhof, W. L. Vos, R. Sprik, and A. Lagendijk, Phys. Rev. Lett. **83**, 2942 (1999).
[12] M. Volanthen, H. Geiger, M. J. Cole, R. I. Laming, and J. P. Dakin, Electron. Lett. **32**, 757 (1996).
[13] E. I. Petermann, J. Skaar, B. E. Sahlgren, R. A. H. Stubbe, and A. Friberg, J. Lightwave Technol. **17**, 2371 (1999).
[14] J. Skaar, Opt. Lett. **24**, 1020 (1999).
[15] M. Galli, D. Bajoni, F. Marabelli, L. C. Andreani, L. Pavesi, and G. Pucker, Phys. Rev. B **69**, 115107 (2004).
[16] B. Soller, D. Gifford, M. Wolfe, and M. Froggatt, Opt. Express **13**, 666 (2005).
[17] S. D. Dyer, IEEE Photonics Technol. Lett. **13**, 230 (2001).
[18] M. Balistreri, H. Gersen, J. Korterik, L. Kuipers, and N. V. Hulst, Science **294**, 1080 (2001).
[19] H. Gersen, T. J. Karle, R. J. P. Engelen, W. Bogaerts, J. P. Korterik, N. F. van Hulst, T. F. Krauss, and L. Kuipers, Phys. Rev. Lett. **94**, 073903 (2005).
[20] A. Bruyant, S. Aubert, G. Lerondel, S. Blaize, R. Bachelot, P. Royer, and V. Minier, in *Engineered Porosity for Microphotonics and Plasmonics Symposium*, edited by R. Wehrspohn, F. Garcia-Vidal, M. Notomi, and A. Scherer (Materials Research Society, Warrendale, PA 2004), p. 243.
[21] R. Bachelot, G. Lerondel, S. Blaize, S. Aubert, A. Bruyant, and P. Royer, Microsc. Res. Tech. **64**, 441 (2004).
[22] V. S. Volkov, S. I. Bozhevolnyi, P. I. Borel, L. H. Frandsen, and M. Kristensen, Phys. Rev. B **72**, 035118 (2005).
[23] L. Weller-Brophy and D. G. Hall, J. Opt. Soc. Am. A **4**, 60 (1987).

[24] Z. H. Wang, G. Penk, and P. Chu, Opt. Commun. **177**, 245 (2000).
[25] M. P. Rouard, *Propriétés Optiques Des Lames Minces Solides* (L'Académie des Sciences de Paris, Paris, 1952).
[26] E. Flück, A. M. Otter, J. P. Korterik, M. L. M. Balistreri, L. Kuipers, and N. Hulst, J. Microsc. **202**, 104 (2000).
[27] A. Nesci, R. Dändliker, and H. P. Herzig, Opt. Lett. **26**, 208 (2001).
[28] J. C. Gates, J. D. Mills, and W. S. Brocklesby, Appl. Phys. Lett. **83**, 1890 (2003).
[29] J. C. Weeber, Y. Lacroute, A. Dereux, E. Devaux, T. Ebbesen, C. Girard, M. González, and A. L. Baudrion, Phys. Rev. B **70**, 235406 (2004).
[30] A. Drezet, A. L. Stepanov, A. Hohenau, B. Steinberger, N. G. H. D. A. Leitner, F. R. Aussenegg, J. R. Krenn, M. U. Gonzalez, and J.-C. Weeber, Europhys. Lett. **74**, 693 (2006).
[31] S. I. Bozhevolnyi and E. Bozhevolnaya, Opt. Lett. **24**, 747 (1999).
[32] S. I. Bozhevolnyi, B. Vohnsen, and E. Bozhvolnaya, Opt. Commun. **172**, 171 (1999).
[33] S. I. Bozhevolnyi, Opt. Commun. **212**, 51 (2002).
[34] M. Balistreri, J. Korterik, L. Kuipers, and N. V. Hulst, J. Lightwave Technol. **19**, 1169 (2001).
[35] A. C. Boccara, Tech. Rep. Contract N88, MRT (1988), n88.
[36] H. Wickramasinghe and C. Williams, *Apertureless Near Field Optical Microscope* U.S. Patent No. N4, 947, 034, 1990.
[37] S. Aubert, A. Bruyant, S. Blaize, R. Bachelot, G. Lerondel, S. Hudlet, and P. Royer, J. Opt. Soc. Am. B **20**, 2117 (2003).
[38] R. Hillenbrand and F. Keilmann, Phys. Rev. Lett. **85**, 3029 (2000).
[39] R. Hillenbrand, B. Knoll, and F. Keilnmann, J. Microsc. **202**, 77 (2000).
[40] I. Stefanon, S. Blaize, A. Bruyant, S. Aubert, G. Lerondel, R. Bachelot, and P. Royer, Opt. Express **13**, 5553 (2005).
[41] S. Blaize, S. Aubert, A. Bruyant, R. Bachelot, G. Lerondel, P. Royer, J. Broquin, and V. Minier, J. Microsc. **209**, 155 (2002).
[42] G. V. Rhodes, B. Goldberg, M. Unlu, S. Chu, W. Pan, T. Kanedo, Y. Kokobun, and B. Little, Appl. Phys. Lett. **75**, 2368 (1999).
[43] A. Bruyant, G. Lérondel, P. Reece, and M. Gal, Appl. Phys. Lett. **82**, 3227 (2003).
[44] S. Blaize, L. Bastard, C. Cassagnetes, G. Vitrant, and J.-E. Broquin, Proc. SPIE **209**, 4640 (2002).
[45] P. Benech and D. Khalil, Opt. Commun. **118**, 220 (1995).
[46] T. Murphy, J. Hastings, and H. Smith, J. Low Temp. Phys. **19**, 1938 (2001).
[47] A. Bruyant, I. Stefanon, G. Lerondel, S. Blaize, S. Aubert, R. Bachelot, P. Royer, P. Pirasteh, J. Charrier, and P. Joubert, Phys. Status Solidi A **207**, 1417 (2005).

[48] J. Walford, J. Porto, R. Carminati, J.-J. Greffet, P. Adam, S. Hudlet, J.-L. Bijon, A. Stashkevich, and P. Royer, J. Appl. Phys. **89**, 5159 (2001).

[49] I. S. Averbukh, B. M. Chernobrod, O. A. Sedletsky, and Y. Prior, Opt. Commun. **174**, 33 (2000).

[50] This assumption is a good approximation in the case of weakly confined modes such as in the ion-exchanged waveguides in glass substrate investigated in the experimental part. For these waveguides, one usually considers a quasi-TE mode (E_z) and a quasi-TM mode (E_y), having slightly different optical constants and very small longitudinal components. Moreover, the eventual contribution of radiation modes due to scattering is not considered in our description. Practically, they can be filtered out by Fourier analysis as shown elsewhere (Ref. 40).

[51] This derivation is correct in careful experimental conditions. The probe has to be symmetric and the detection direction must be perpendicular to the propagation direction of the two guided modes. These two points are mandatory in order to have the same sensitivity for the forward and reflected guided modes (i.e., the same transfer function).

[52] The value of the effective index can be read for each wavelength by measuring the averaged standing-wave periodicity. However, for the ion exchanged waveguide, the effective index dispersion is too small to be measured on a standard scanning range.